Electronic Supplementary Material (ESI) for Analyst.

A Micro Passive Preconcentrator for Micro Gas Chromatography

Changhua Zhan,[1,4] Muhammad Akbar,[1,4] Robert Hower,[1,4] Nicolas Nuñovero,[1,4] Joseph Potkay,[2,4*] Edward T. Zellers,[1,3,4*]

[1] *Department of Environmental Health Sciences, University of Michigan, Ann Arbor, MI, USA*

[2] *Department of Surgery, University of Michigan, Ann Arbor, MI, USA*

[3] *Department of Chemistry, University of Michigan, Ann Arbor, MI, USA*

[4] *Center for Wireless Integrated MicroSensing & Systems (WIMS^2), University of Michigan, Ann Arbor, MI, USA.*

Corresponding authors: ezellers@umich.edu,; jpotkay@umich.edu

The following sections of this Electronic Supporting Information file present details related to the corresponding topics presented in the main article:

S1. µPP fabrication; µPCF description

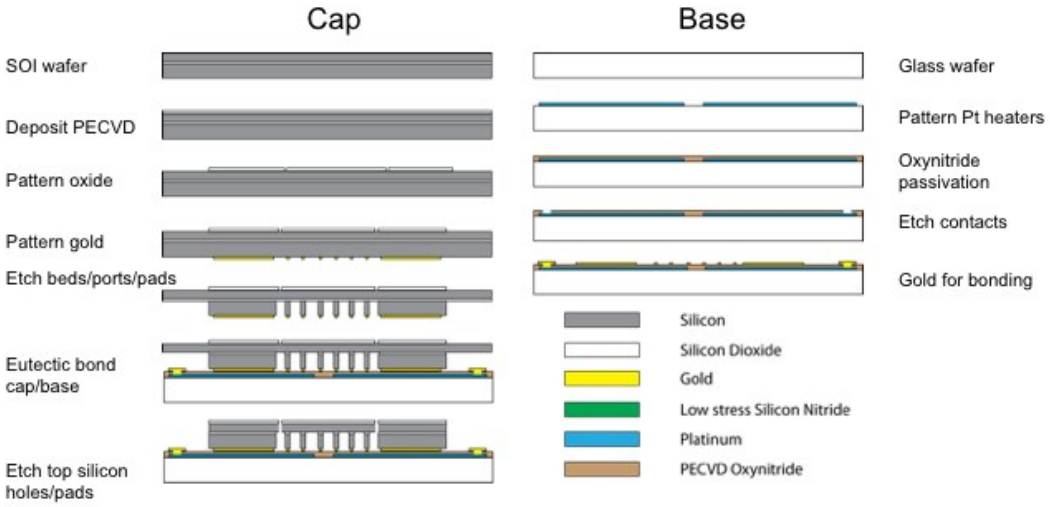

Figure S1. Summary of the fabrication process flow for the µPP device. Top SOI wafer layer thicknesses: device layer, 180µm; buried oxide layer, 1.5µm; handle layer, 380 µm. Bottom borofloat glass thickness was 200 µm.

The µPP fabrication process flow is summarized in Figure S1. The thicknesses of the three layers of the 4" silicon-on-insulator (SOI) wafer used to create the top substrate of the µPP are given in the caption of Figure S1. First, a 1-µm thick silicon dioxide layer was deposited onto the top of the device-layer side of the SOI wafer using plasma enhanced chemical vapor deposition (PECVD). Photoresist was then deposited and patterned (i.e., exposed) to define the circular array (i.e., ring) of sampling apertures at the periphery of the active device area (o.d. ≈ 4.3 mm). Each aperture was defined as a 50 × 50 µm square spaced from laterally adjacent apertures by 75 µm. Two concentric rings of apertures (120 outer, 100 inner) were patterned, and then an additional 17 apertures were added, evenly distributed just outside the outer ring to bring the total to 237 apertures (see Figures 1f and g in the main article for micrographs of the apertures). In the same step, the rectangular regions at the corners of the chip, corresponding to where the wire-bonding areas are located on the bottom substrate, were patterned. All exposed regions of PECVD oxide were then removed by reactive ion etching (RIE).

Next, a seed layer of Au was deposited onto the back (i.e., handle layer) side of the SOI wafer, patterned with photoresist and electroplated to a thickness of ~2 µm using a standard plating bath in the exposed areas. The Au seed layer was then stripped. Next, photoresist was patterned to define the adsorbent-bed cavities, retention pillars, wire-bonding regions, fill ports, and fluidic channel (please refer to Figure 1e and f in the main article) and these features were formed by deep-reactive-ion etching (DRIE) down to the buried oxide layer. Finally, the exposed buried oxide was etched away with buffered HF to ensure that when the aperture grid was later etched from the top side that the apertures extend through the top substrate.

Figure S2 shows the top substrate of the chip after DRIE. The pillars are ~180 μm in diameter and spaced by ~130 μm. The three fill ports and the fluidic channel are 460 and 170 μm wide, respectively, at their narrowest points. The height of all features is 380 μm.

The first step in processing the bottom (glass) wafer entailed depositing photoresist, patterning (exposing) the locations for the heaters, RTDs, and electrical traces out to the wire-bonding areas on the top surface. Ti and Pt at thicknesses of 100Å and 1000Å, respectively, were deposited and a standard lift-off procedure was used to remove the unwanted metal. A 2-μm thick SiON (oxynitride) layer was then deposited by PECVD to serve as an electrical isolation layer. Next, the contact holes were patterned using photoresist and the oxynitride was etched away with buffered HF to expose the Pt metal for eventual wire bonding. Finally, a thin Au film was deposited and patterned by lift-off at the locations matching those of the top substrate needed for eutectic bonding (see Figure S3 for a micrograph of a portion of the bottom substrate prior to bonding).

The top and bottom substrates were then aligned using a contact aligner and bonded using Au-Si eutectic bonding.[S1] The apertures and wire-bonding regions previously patterned in the oxide on the top surface of the top substrate were then etched by DRIE using the remaining oxide as the etch mask. Finally, the wafers were diced using a dicing saw, and thoroughly cleaned using organic solvents, yielding devices such as that shown in Figure 1f (main article).

Note that the heater in the center of the chip and along the fluidic transfer channel were not used. An additional chip heater and RTD encircling μPP structure and intended for heating the chip outside of the active device area was also found to be unnecessary due to conductive heat transfer through the substrates.

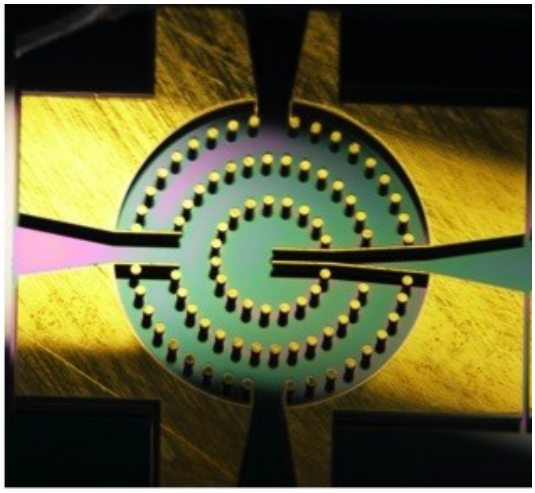

Figure S2. Top substrate prior to wafer bonding, showing adsorbent cavities, adsorbent retention pillars, fill ports (3), and fluidic channel (right side). Au layer is where eutectic bonding to the bottom substrate will occur.

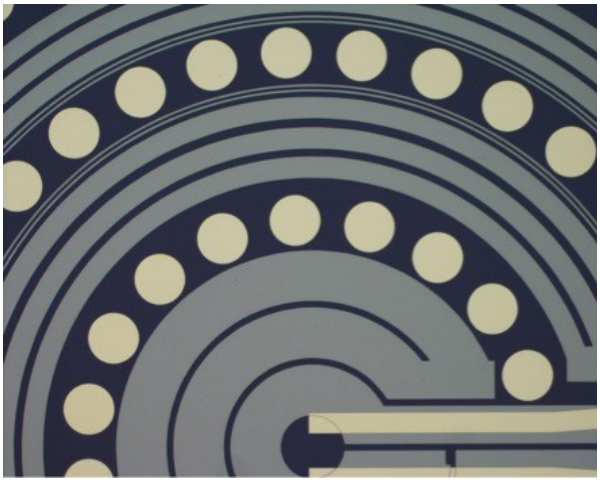

Figure S3. Borofloat glass bottom substrate with heaters shown in gray and Au layer at the bases of the pillars and fluidic port where eutectic bonds will occur in white.

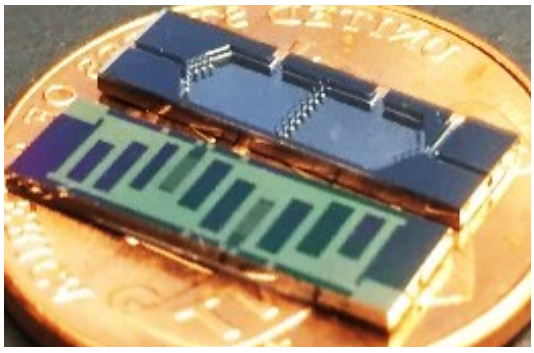

Figure S4. Photo of μPCF. Lower image is the backside heater and upper image shows the two adsorbent cavities, fill ports, and fluidic channels of the unfilled device. See ref. S2 for more fab details. The tandem adsorbent cavities contain ~2.3 mg each of C-X and C-B separated and retained within the chambers by pillars. An etched tee-junction at one end of the μPCF chip allows for vapor loading in one flow direction and desorption/injection in the other (i.e., with backflushing) by use of an integrated, thin-film heater on the backside operated under closed-loop control.

S2. Test system and exposure chamber

The test atmosphere generation system and associated components are shown schematically in Figure S5. The custom-made stainless-steel exposure chamber (12.7 × 7.6 × 3.9 cm; ~42 mL internal volume) used to house the µPP for performance tests is shown in Figure S6 with the cover plate (top layer) removed. The bottom plate has tapped inlet and outlet holes for gas flow, flanking a central 1"-diameter clearance hole for electrical interconnections between the PCB-mounted µPP and a routing PCB bolted to the underside of the bottom plate and sealed with a Teflon o-ring. The 11 contact pins on the routing PCB passing vertically through the central hole of the chamber floor plate serve as mechanical supports for the µPP carrier PCB "pedestal" and as the electrical interconnects.

The middle plate of the chamber was machined to create a chamfered diamond shaped cavity that defines the internal volume. A tapped hole in the side of the middle plate of the chamber accepts a PEEK fitting with a reverse ferrule that seals the (Microlumen-wrapped) µPP outlet capillary to the chamber wall. The outlet capillary extends through this fitting to one of the 6-port valve ports for directing the flow from the µPP to the µPCF during desorption and sample transfer. Teflon gaskets are used to seal the top and bottom plates to the middle plate with compression provided by a set of nuts and bolts.

At a flow rate of 1 L/min, the atmospheric concentration in the chamber can reach 95% of the equilibrium concentration within ~2 min for m-xylene, as indicated by GC-FID measurements. The theoretical 95% mixing time is about 10 sec. The longer time required in practice maybe due to adsorption by the upstream 3-way solenoid valve. Consistent with this explanation, for less volatile test compounds, such as DEMP, the time to steady-state concentration was longer (i.e., ~4 min). After exposure, the testing chamber was purged with N_2 for 4 min at 1 L/min, which was sufficient to remove any trace of residual vapor.

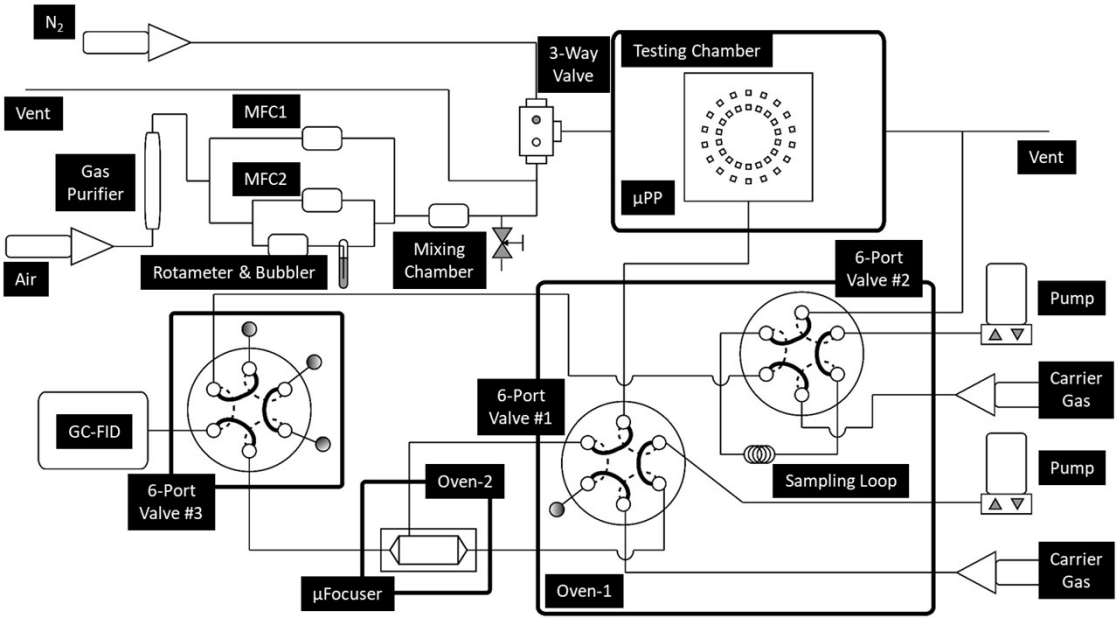

Figure S5. Diagram of the μPP test system. The three six-port valves can be switched to achieve the following three functions: 1) monitoring the concentration and composition of the test-chamber atmosphere; 2) transferring collected samples from the μPP to μPCF; 3) analyzing samples injected from μPCF by GC-FID.

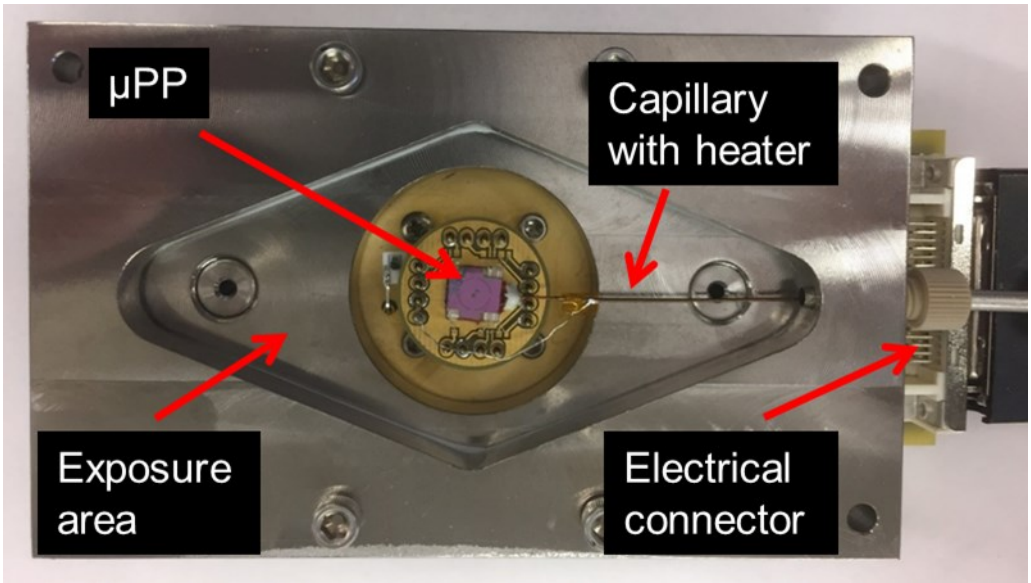

Figure S6. Photo of the exposure chamber with μPP mounted inside it.

S3. TGA set-up and procedure

The TGA was used to measure the equilibrium adsorption capacity, W_e, of selected vapors as a function of concentration for each adsorbent material. The test atmosphere generation system described above was adapted for these experiments by directing the flow through tubing connected to the sample chamber within the TGA to allow real-time mass measurements during exposure, N_2 purge, and then heating to desorb the vapors. For most tests, ~2.6-2.9 mg of the sieved adsorbent material (i.e., C-X or C-B) was loaded into the standard weighing pan of the TGA and suspended from the arm of the gravimetric mechanism. It was then heated to 250 °C under a flow of N_2 to precondition the sample for > 30 min.

The flow of test atmosphere was divided so that a portion would flood the chamber containing the sample and a portion was sent to a sampling loop connected to a 6-port valve mounted on the GC. Samples were periodically injected into the GC over the course of each exposure to confirm the magnitude and stability of the exposure concentration. Since testing involved only individual compounds no column was used. Rather, a short segment of deactivated fused silica capillary (guard column) was used to connect the injection port to the FID.

For isotherm determinations, each concentration was tested individually and the mass uptake was monitored until a plateau was reached followed by thermal desorption to confirm recovery of the baseline. Then the next concentration was tested. Equilibration times were on the order a few hrs. For other tests, exposures were allowed to proceed for a certain time period, then an N_2 purge was used to remove the vapor so that any off-gassing could be detected, and then the sample was heated to confirm recovery of the baseline.

S4. Temperature profiles

A typical time-temperature profile for each of the three RTDs on the μPP is shown in Figure S7. Closed-loop control of the two cavity heaters allows precise control and coordination of the temperatures in both adsorbent beds. Modest heating rates were used so that it took about 6 sec to achieve the maximum temperature with no overshoot.

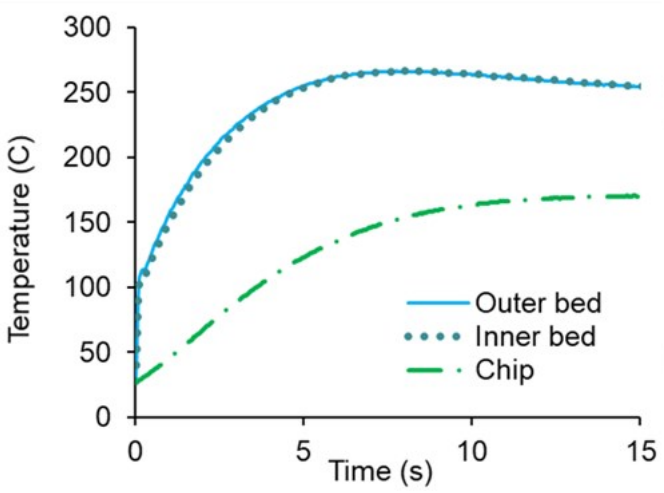

Figure S7. Profiles from the RTD readings for one heating sequence of the inner and outer adsorbent cavities, as well as the chip area (outside of the cavities) of the μPP device.

S5. TGA data and W_e values

Most studies of VOC adsorption on carbon adsorbents employ models based on the classical Langmuir adsorption isotherm: [S3-S8]

$$W_e = W_{e-max} \frac{b \times C}{1 + b \times C} \quad \text{(S-1)}$$

where $W_{e\text{-}max}$ is the maximum monolayer coverage capacity (μg/g), b is the Langmuir isotherm constant (L/mg), and C is the VOC concentration (mg/m^3).

Figure S8 shows the adsorption isotherm for m-xylene on C-X over a concentration range of 0.9 to 1300 mg/m^3. The W_e value increased with the increasing m-xylene concentration at a steadily decreasing rate and the isotherm was fit to the following Langmuir model, represented by the curve in Figure S8 ($r^2 = 0.936$):

$$W_e\,(\mu g/g) = \frac{61000\,(\mu g/g) \times 25\,(L/mg) \times C\,(mg/m^3)}{1 + 25\,(L/mg) \times C\,(mg/m^3)} \quad \text{(S-2)}$$

Figure S9 shows that W_e is inversely proportional to the vapor pressure among four vapors of similar polarity with C-X: toluene, m-xylene, 1,2,4-TMB and n-decane at similar concentrations (4-6 mg/m^3).

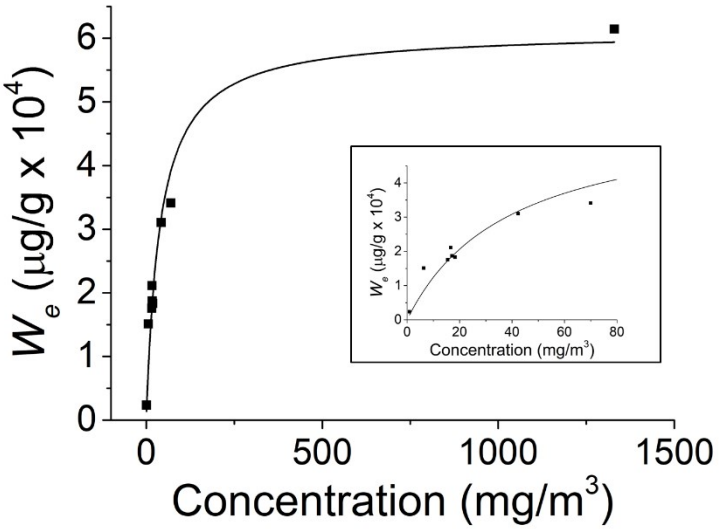

Figure S8. W_e values of C-X for exposure to different concentrations of m-xylene. The curve is the fitted to the Langmuir model in eq. S-2 (R^2 = 0.96). Inset shows and enlargement of the lower concentration region.

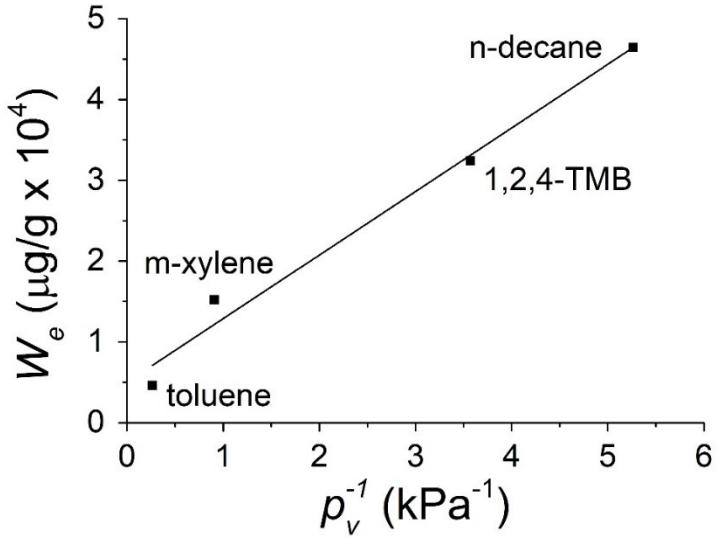

Figure S9. W_e values of several VOCs with C-X as a function of 1/(vapor pressure). Vapor pressures of toluene, m-xylene, 1,2,4-TMB, and n-decane are 3.8, 1.1, 0.28, and 0.19 kPa, respectively (R^2 = 0.98).

Table S1. Values of $M_{b\text{-}10}$ for several compounds obtained in published breakthrough tests with C-B and C-X, and the corresponding W_e values at 3.5 mg/m³ derived therefrom. Also included are the estimates of maximum uptake masses on the C-B bed of the µPP at 3.5 mg/m³ for the same compounds.

Compound	$M_{b\text{-}10}$[a] (µg)		W_e[b] (µg/g)		C-B Max. Uptake Mass (ng)
	C-B	C-X	C-B	C-X	
m-xylene	12		1700	4900	1000

o-xylene			2100	6100	1300
DMMP	3.9	11	550	1600	340
DEMP	11		1600	4500	950
DIMP	16		2300	6500	1400
NBZ	24		3400	9800	2100
n-butanol		1.3	---[c]	190	---[c]

[a] $M_{b\text{-}10}$ values are the 10% breakthrough masses reported in ref. S9; [b] W_e value estimation processes are discussed in the text; [c]experimental testing reported in ref. S9 showed n-butanol to be unretained on C-B.

TGA testing of the lower volatility compounds DMMP, DEMP, DIMP, and NBZ was not possible due to their adsorption on surfaces and persistence. Therefore, we used alternative methods to estimate W_e values.

In a separate study of vapor adsorption capacity, we conducted conventional breakthrough tests with packed tubes containing either C-B or C-X exposed continuously to each of several individual test compounds at a single vapor concentration.[S9] Most compounds were only tested with C-B. Measured 10% breakthrough volumes ($V_{b\text{-}10}$) were converted to the corresponding 10% breakthrough masses ($M_{b\text{-}10}$) to account for the different challenge concentrations used. Theoretically, $M_{b\text{-}10}$ for a given compound should be proportional to W_e according to the Wheeler Model.[S9] Using m-xylene as the reference compound, the following values of relative $M_{b\text{-}10}$ values were found for breakthrough tests with C-B: 1.0, 0.33, 0.92, 1.3, and 2.0 for m-xylene, DMMP, DEMP, DIMP, and NBZ, respectively.

For one of these compounds, DMMP, we also ran breakthrough tests with C-X, and the C-X:C-B ratio of $M_{b\text{-}10}$ values for DMMP was 2.9 at the same concentration. Assuming that this ratio would be applicable to other vapors, we applied it to the W_e value of m-xylene on C-X at 3.5 mg/m^3 determined by TGA to obtain an estimate of W_e on C-B for m-xylene. This specific concentration was arbitrary. Combining this estimate of W_e with the ratios listed above, it was possible to estimate W_e on C-B for the other vapors at the same concentration. Breakthrough tests of n-butanol with C-B showed no retention (i.e., immediate breakthrough), whereas with C-X the n-butanol breakthrough volume (mass) was short but measurable, thereby permitting an estimate of W_e.[S9]

Based on the estimated W_e values and the measured adsorbent masses, we could also estimate the equilibrium uptake mass for each compound on C-B (the adsorbent in the outer bed of μPP). These estimates of W_e and uptake mass are presented in Table S1 and were used in the modeling discussed further below.

The W_e value of o-xylene on C-X was estimated from that of m-xylene at a similar concentration via the plot in Figure S9 by assuming that its W_e value is proportional to the inverse of vapor pressure, which should be valid for compounds with similar polarities (or, in this case, for an isomer). The W_e value of o-xylene on C-B was then estimated, as described above, using the ratio of W_e values on C-X and CB found for DMMP (i.e., 2.9, see above).

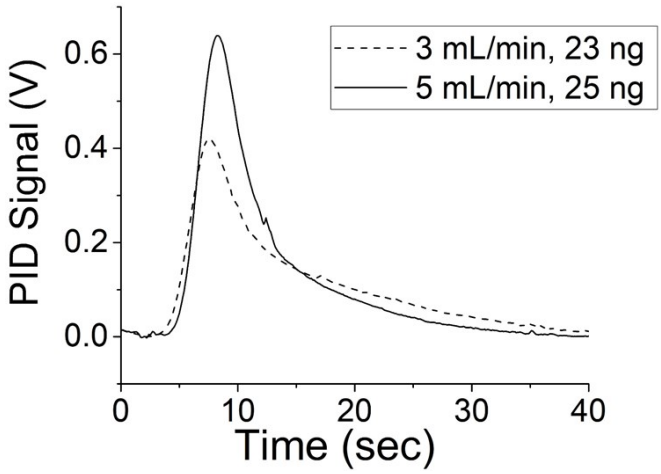

S6. Desorption (transfer) profiles and efficiencies

Figure S10. Desorption profiles of o-xylene from the μPP under the two indicated flow rates at 250 °C as measured with an in-line photoionization detector (mini-PID). The indicated masses collected from the test atmosphere were determined. Challenge concentrations were ~ 12 mg/m³.

To characterize the transfer of o-xylene from the μPP during desorption, we connected a mini-PID between the mini-pump and the outlet of the μPP. Two tests were performed at a similar exposure concentrations and exposure times, but at different desorption flow rates (i.e., 3 mL/min and 5 mL/min). Two consecutive desorption cycles were performed in each case and no desorption peak was observed for the second desorption cycle, confirming that desorption was efficient. The collected masses were similar between two tests as expected. As shown in Figure S10, the profile showed significant tailing but the responses returned to baseline within about 30 sec. The full width at half maximum (FWHM) was 5.7 and 4.7 sec at 3 and 5 mL/min, respectively.

Tables S2 and S3 show the results of desorption tests with DMMP and DEMP, respectively. The *DE* values for DMMP were > 97% under all conditions. For DEMP, the *DE* at 250 °C was 85% (data not shown). Increasing T_{max} to 275 °C improved the *DE* to 94%. At this T_{max}, reducing the transfer time from 60 to 30 sec, resulted in a decrease in *DE* to 78%. Thus, 60 sec at 275 °C at 5 mL/min seemed to be the best condition for transfer.

Table S2. The sampling rates and desorption efficiencies (DE) of μPP at 250 °C for DMMP with different transfer conditions (transfer flow rate and transfer time).[a]

S_e (mL/min)	Transfer flow rate (mL/min)	Transfer time (sec)	DE (%)
0.44	10	240	100

0.44	10	120	98
0.43	10	60	97
0.44	5	60	99

[a] *Exposures ranged from 24-30 mg/m³ for 15 min resulting in mass uptakes of 160-200 ng*

Table S3. The sampling rates and desorption efficiencies of μPP at a transfer flow rate of 5 mL/min and transfer temperature of 275 °C for DEMP with different transfer time.

S_e (mL/min)	Transfer time (sec)	DE (%)
0.26	60	94
0.26	50	89
0.25	40	79
0.25	30	78

[a] *Exposures ranged from 54-63 mg/m³ for 15 min for a total mass load of 210-230 ng.*

Table S4. Results of μPP off-gassing tests for o-xylene, DMMP, and DEMP with 4 min and 60 min purge times after exposure.

Compound	Purge time (min)	Conc. (mg/m³)	Uptake mass (ng)	S_e (mL/min)	S_e change (%)
o-xylene	4	52	530	0.67	-6.0
	60	59	560	0.63	
DMMP	4	49	320	0.43	-19
	60	47	245	0.35	
DEMP	4	57	210	0.25	0
	60	52	190	0.25	

S7. Modeling changes in S_e values as a function of time and concentration

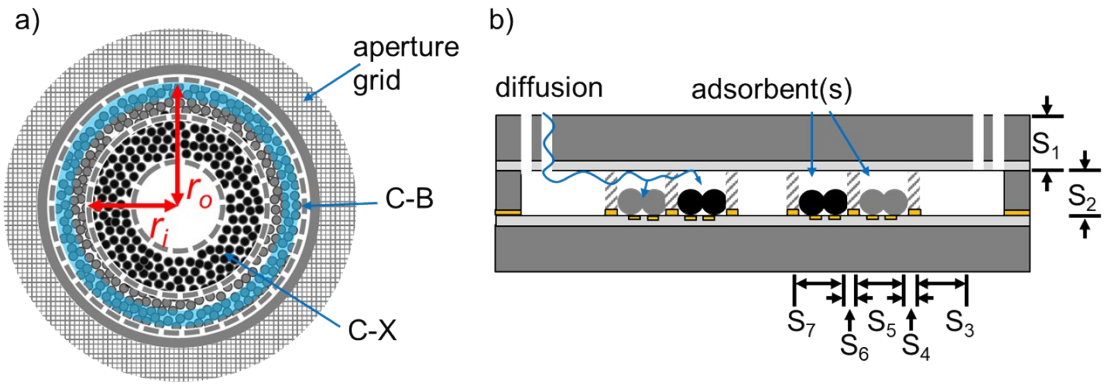

Figure S11. a) Top view of μPP showing radii and adsorbent beds (the blue annulus corresponds to a hypothetical saturated C-B area at a certain time point); b) Enlarged version of Fig. 1b (main text) showing a side view of formalized segments of the diffusion path and individual sampling rates (S_1-S_7).

As stated in the main text, to model the effective sampling rate for a given vapor, we formally divided the diffusion path into 7 segments as shown in Figure S11. Each segment is defined as follows:

- Segment 1 corresponds to the aperture grid through which vapors diffuse vertically and for which L_1 is the thickness of the top substrate and A_1 is the product of the aperture cross section (47 × 47 μm) and the number of apertures (n = 237).
- Segment 2 corresponds to the space beneath the apertures through which vapors will also diffuse vertically to the floor of the bottom substrate, for which L_2 is the height of the channel (380 μm) and A_2 is defined to include the total area of the aperture grid and the spaces between the apertures. Thus, Segment 2 corresponds roughly to the volume of the annular ring beneath the grid of apertures.
- Segment 3 corresponds to the open space adjacent to (just inside of) Segment 2 through which vapors diffuse laterally (inwardly) toward the first ring of retention pillars. For this segment we assume that L_3 is the distance from the edge of Segment 2 to the pillars, and A_3 is the average cross section of the lateral path but at only at the height of adsorbent granules (237 μm). The formal assumption here is that the headspace has no vapor.
- Segment 4 is the path through the pillars for which L_4 is the diameter of a pillar and A_4 is the sum of the inter-pillar distances multiplied by the height of the adsorbent granules.
- Segment 5 is the outer (C-B) adsorbent bed through which vapors diffuse laterally. In this case diffusion will be some combination of free (i.e., Fickian) diffusion through the interstitial spaces between the particles and pore (i.e., Knudsen) diffusion within the adsorbent particles. Therefore, the D value in this segment is assumed to be lower than that in the preceding segments. L_5 is the radial length of entire C-B adsorbent bed, which is only reached by vapor after saturation of the entire adsorbent bed. A_5 decreases physically from the outer to inner boundaries of the adsorbent bed. As with the radial length, the effective value of A_5 over the course of a sampling period will depend on the extent of bed saturation. S_5 will decrease over time and, therefore S_e will also decrease over time.
- Segment 6 corresponds to the next set of pillars and its dimensions are defined similarly to that of Segment 4, accounting for the lower number of pillars at this point in the device structure.
- Segment 7 is the inner (C-X) adsorbent bed. As in Segment 5, diffusion will be some combination of free (i.e., Fickian) diffusion through the interstitial spaces between the particles and pore (i.e., Knudsen) diffusion within the adsorbent particles. Therefore, the D value in this segment is also assumed to be lower than that in segments not containing adsorbent. L_7 is the radial length of entire C-X adsorbent bed, which is only reached by vapor after saturation of the entire adsorbent bed. A_7 decreases from the outer to inner boundaries of the adsorbent bed. As with the radial length, the effective value of A_7 over the course of a sampling period will depend on the extent of bed saturation. Since S_7 will decrease over time, it will contribute to a decrease in S_e for vapors penetrating this bed.

As discussed in the main text, the response time can be estimated by first dividing the volume of each segment *S1-S4* its modeled S_i value (i = 1, 2, 3, 4), and then summing the resulting segmental response time values. See Table S5 for the relevant values for o-xylene.

Table S5. Segmental effective sampling rates (S_i) and volumes relevant to the calculation of the response time (i.e., time to steady state) of the μPP for o-xylene.[a]

Segment	S_i (mL/min)	Volume (mm^3)	Response Time (msec)
1	1.3	0.094	4.5
2	2.6	0.86	20
3	13	0.18	0.84
4	3.6	0.27	4.5
		Total	30

[a] *Similar calculation for DEMP and DIMP gave values of 60 msec and 77 msec, respectively.*

Implicit assumptions in eq. 1 (main text) are that, once steady state is established, all of the S_i values are constant and all vapor mass transferred into the device is conserved. If S_i in any segment changes, then it will have a commensurate effect on S_e. Importantly, eq.1 gives the *instantaneous* S_e at a certain point in time. If S_e were to change with time, then a time-averaged S_e value over the duration of the sampling period would be observed experimentally. Accordingly, the corresponding modeled value would also be averaged over time.

Next we model the instantaneous sampling rates (S_5 and S_e) as a function of time, and then calculate the net time-averaged S_e values over a specified sampling period. We focus on the effect on S_e of the gradual saturation of the adsorbent in segment 5 (S5) that occurs either over time at a given concentration of vapor or over a range of vapor concentrations at a fixed sample duration. Analogous expressions are used to model S_7. Considering S_5 in isolation, we have the formal expression: $S_5 = D_5A_5/L_5$. However, since the effective values of A_5 and L_5 will vary with time and the degree of saturation, we have designated them as l_s and a_s. It is assumed that D_5 is constant.

To develop the model, we considered the case where the μPP collects a series of samples over several discrete time periods and transfers the collected mass downstream for analysis (as in Figure 4 for o-xylene). For each time, t, an injected mass of vapor is measured, $m_{v(t)}$. Assuming that the penetration into the bed proceeds only after saturation is achieved in the adjacent upstream fraction of the bed at a given air concentration, we can estimate the saturated adsorbent mass ($m_{s(t)}$) corresponding to each value of $m_{v(t)}$ by the following:

$$m_{s(t)} = \frac{m_{v(t)}}{W_e} \tag{S-3}$$

where W_e is the equilibrium adsorption capacity at a given concentration C_0 (see Section S5).

We can also estimate the maximum vapor mass required to saturate the bed, $m_{v\text{-}max}$, at a given C_0 by the product of W_e and the total bed mass, $M_{a\text{-}max}$. We can then determine what fraction of the adsorbent bed, $f_{s(t)}$, is saturated after each time period as

$$f_{s(t)} = \frac{m_{s(t)}}{M_{a-max}} \tag{S-4}$$

The total bed area, which we call $\Lambda_{a\text{-}max}$ (to differentiate it from the cross sectional area of the diffusion path, A), is obtained from the CAD design layout for the device. Multiplying $f_{s(t)}$ by $\Lambda_{a\text{-}max}$ gives the area of the bed, $\alpha_{s(t)}$, saturated at time t. Assuming $\alpha_{s(t)}$ is evenly distributed around the perimeter of the bed, P, it would consist of an annulus of adsorbent of radial length $l_{s(t)}$. At the point where the adsorbent bed is fully saturated, $l_{s(t)}$ would equal L_5. Since $\Lambda_{a\text{-}max}$ is the sum of the areas of the saturated and unexposed bed, we have:

$$\Lambda_{a-max} = \alpha_{s(t)} + \pi(r_o - l_{s(t)})^2 - \pi r_i^2 \tag{S-5}$$

where r_o and r_i are outer and inner radii of the (outer, C-B) adsorbent bed, respectively. Rearranging this equation, we have the following, which can be used to obtain the value of $l_{s(t)}$ for each $\alpha_{s(t)}$ corresponding to exposure for any discrete time period:

$$l_{s(t)} = r_o - \sqrt{\frac{\Lambda_{a-max} - \alpha_{s(t)} + \pi r_i^2}{\pi}} \tag{S-6}$$

Of course, l_s and α_s change continuously with time, and can be expressed as continuous variables. Within an incremental time interval dt there will be incremental increases in adsorbed vapor mass (dm_v), saturated adsorbent area ($d\alpha_s$), and saturated radial length (dl_s). Furthermore, the following equality should hold:

$$\frac{dm_v}{m_{v-max}} = \frac{d\alpha_s}{\Lambda_{a-max}} \tag{S-7}$$

and $d\alpha_s$ can be expressed as the product of the perimeter of the unexposed bed (P_u) and dl_s as follows:

$$d\alpha_s = P_u dl_s = \pi(2r_o - 2l_s)dl_s \tag{S-8}$$

Assuming S_e is constant within this interval, then dm_v can be expressed as follows:

$$dm_v = S_e C_0 dt \tag{S-9}$$

Limiting this analysis to the first five segments, eq. 1 (main text) can be expressed as follows:

$$S_e = \frac{1}{\frac{1}{S_1}+\frac{1}{S_2}+\frac{1}{S_3}+\frac{1}{S_4}+\frac{1}{S_5}} = \frac{1}{\frac{L_1}{DA_1}+\frac{L_2}{DA_2}+\frac{L_3}{DA_3}+\frac{L_4}{DA_4}+\frac{l_s}{D_5 a_s}} \tag{S-10}$$

where D is the Fickian diffusion coefficient (listed in Table 1 of the main text), and D_5 is the diffusion coefficient in S5, which is assumed to be smaller than D by virtue of the contribution of (slower) pore diffusion (see above), and a_s is the cross-sectional area at the inner edge of the saturated region of the bed. The latter is the product of P_u and the height of adsorbent bed (h):

$$a_s = P_u h = \pi(2r_o - 2l_s)h \tag{S-11}$$

Since S_1-S_4 are constant at steady state, Eq. S-10 can be simplified to:

$$S_e = \frac{1}{\sigma_{1-4} + \frac{l_s}{D_5 h\pi(2r_o - 2l_s)}} \tag{S-12}$$

where $\sigma_{1\text{-}4} = 1/S_1+1/S_2+1/S_3+1/S_4$.

Substituting the expression for S_e in Eq. S-10 into Eq. S-9, and then substituting the expressions for $d\alpha$ and dm_a in Eqs. S-8 and S-9 into Eq. S-7 and rearranging gives:

$$\frac{\Lambda_{a-max}\, C_0}{m_{v-max}\,\pi} dt = \left[(2r_o - 2l_s)\sigma_{1-4} + \frac{l_s}{D_5 h\pi}\right] dl_s \tag{S-13}$$

Eq. S-13 has only two variables, t and l_s. All the other parameters in the equation are constant (note: D_5 is also a constant, but its value is unknown). Thus, the left-hand side is integrable with respect to t, and the right-hand side is integrable with respect to l_s.

Imposing the boundary condition that $l_s = 0$ when $t = 0$ and integrating both sides of eq. S-13 gives an equation relating l_s to t wherein all the determinant variables are known except for D_5:

$$\frac{\Lambda_{a-max}\, C_0}{m_{v-max}\,\pi} t = 2r_o\sigma_{1-4} l_s + \frac{l_s^2}{2}\left(\frac{1}{D_5 h\pi} - 2\sigma_{1-4}\right) \tag{S-14}$$

The required value of D_5 must be determined empirically for each vapor. For o-xylene, for example, experimental values of $l_{s(t)}$ were calculated via Eq. S-6 for each of the six cases shown in Figure 4 (main text) for which $m_{v(t)}$ values were measured at each t. The corresponding

modeled values of l_s are expressed in Eq. S-14 as a function of D_5 for each case at the same (known) value of t. Thus, each discrete modeled value $l_{s(t)}$ now depends only on D_5. By iteratively solving Eq. S-14 using D_5 values ranging incrementally from 0 (lower bound) to the Fickian D value (upper bound, i.e., 0.072 cm^2/sec for o-xylene), the optimal value was determined as that providing smallest relative error between modeled l_s values at time t and experimental $l_{s(t)}$ values.

For o-xylene, the resultant value of D_5 was 0.025 cm^2/sec and for DEMP the D_5 value obtained by the same approach was 0.015 cm^2/sec. With these optimized D_5 values and Eq. S-14, we can model l_s for any t assuming the vapor is retained in the C-B bed. By substituting the modeled l_s value into Eq. S-12, we can then obtain the modeled instantaneous S_e value for any t, again, assuming the vapor is retained in the C-B bed.

For comparison with experimental S_e values, we need to determine the time-averaged S_e value over a certain time period. A sufficiently accurate estimate can be obtained by calculating S_e at each 1-minute interval via eq. S-12, summing, and dividing by the total time. The modeled results for DEMP and o-xylene are presented alongside the experimental S_e values in Figures 4 and 5, respectively, in the main text.

An analogous approach would be used to estimate D_7 in the C-X bed for any vapors that penetrate beyond the C-B bed during sampling. In fact, for o-xylene, the model predicts penetration into the C-X bed after ~14 hr at the modeled concentration of 3.5 mg/m^3. Since we did not have the data required to estimate D_7 in the same manner as we estimated D_5, it was assumed that D_7 was equivalent to D_5. For the purpose of modeling the 24-hr Se value presented in Figure 5 (main article). Given the higher specific surface area and packing density, as well as the different pore-size distribution of C-X (vs. C-B), it is likely that D_7 would be somewhat lower than D_5. Accordingly, the model underestimates S_e for the 24-hr sample of o-xylene.

Thus far, we have only dealt with modeling how the sampling rate changes with time. Using the same approach, it is possible to model the S_e as a function of concentration for a fixed time period. The same optimized D_5 value can be used. For any specified concentration, C_0, we need to calculate the corresponding W_e value from TGA measurements or by the approach described above from breakthrough testing. This, then, will give a new $m_{v\text{-}max}$ value. With C_0 and $m_{v\text{-}max}$ values, we can use eq. S-14 to model l_s at any t, followed by calculation of the instantaneous and time-averaged S_e values via eq. S-12. The results for o-xylene are shown in Figure 3 (main article).

Unfortunately, modeling S_e for an untested compound would not be possible because of the need for an optimized D_5 value, which must be derived empirically as we did above. As we discuss in the next section, for o-xylene and DEMP the ratios of the Fickian D value to the D_5 value were 2.9 and 2.4 respectively (i.e., 0.072/0.025 and 0.036/0.015, respectively). Assuming that the average ratio for these two compounds (i.e., 2.7) could be applied to any other compound, we could then estimate D_5 for untested vapors for which we have Fickian D values. For the few cases in Table 1 of the main text for which we had W_e values, we used this approach to model their 0.25-hr S_e values. However, due to the short time period the change in S_e as a function of time was too small to allow an assessment of the reliability of this approach to estimating D_5.

S8. Calculations of Fickian diffusion coefficients (D)

Fickian *D* values were obtained from the literature for six of the compounds listed in Table 1 (i.e., m-xylene, o-xylene, NBZ, DMMP, n-butanol, and DMF).[S10-S12] Since published values could not be found for the remaining nine compounds, they were calculated by one of two methods.[S10,S13-S15] One of these, Fuller's method, has shown the best agreement with experimental values (generally < 10 %, although errors as large as > 60% have been reported).[S10] This method was used to estimate Fickian *D* values for all but two of the compounds for which published *D* values were lacking. The exceptions are the two phosphonates, DEMP and DIMP, for which the requisite atomic diffusion volumes have apparently not been reported. Therefore, an alternative method was used to calculate *D* values for these compounds.[S15]

In Fuller's method, the *D* value (torr cm^2/sec) of vapor A in gaseous matrix B (i.e., D_{AB}) is expressed as follows:[S11]

$$D_{AB} = \frac{1.0868T^{1.75}}{\sqrt{\frac{2m_A m_B}{m_A + m_B}}(\sqrt[3]{V_A} + \sqrt[3]{V_B})^2} \quad \text{(S-15)}$$

where T is temperature (K), V_A and V_B are the so-called molecular diffusion volumes of A and B, and m_A and m_B are their respective molecular weights. B is air in this study. The molecular diffusion volume is the sum of the atomic diffusion volumes of the atoms comprising the molecule, weighted by an adjustment factor related to the structure of the molecule (e.g. branching, aromatic ring, or heterocyclic ring). Values of the atomic diffusion volumes and the structural weighting factors can be found.[S10,S13,S14] Atmospheric pressure was assumed to be 760 torr when converting D_{AB} values to units of cm^2/sec.

For DEMP and DIMP, an alternative method was used, which expresses D_{AB} as follows:[S14]

$$D_{AB} = \frac{1}{3n\sigma_{AB}m_A}\sqrt{\frac{8kLT}{\pi}\left(\frac{m_A m_B}{m_A + m_B}\right)} \quad \text{(S-16)}$$

where L is the Avogadro constant, n is the concentration of air molecules, σ_{AB} is the effective collision cross section, and k is Boltzman constant. To calculate D_{AB} values for DIMP and DEMP, we need to know the values of parameters on the right-hand size of the equation. All parameters in this equation are available from the literature except for σ_{AB}.[S16] To estimate σ_{AB} value, a molecular modelling package (VEGA ZZ)[S17] was used to obtain the molecular volumes of DEMP and DIMP. Assuming their molecules to be spherical, the molecular diameters can be estimated and a σ_{AB} value for DEMP and DIMP can be obtained.

As a check on the accuracy of eq. S-16, D_{AB} values of DMMP and m-xylene in air were calculated using this equation and compared to those reported in the literature or calculated by use of Fuller's method. Using eq. S-16, the D_{AB} values for DMMP and m-xylene are 0.015 cm^2/s and 0.017 cm^2/s, which are 30% and 25% of the reported D_{AB} values, respectively. Thus, it appears that eq. S-16 significantly underestimates D_{AB}. To account for this, we used 0.3 as an adjustment factor and used it to re-calculate the D_{AB} values of DEMP and DIMP, i.e., we divided the estimated D_{AB} values of DEMP and DIMP based on the eq. S-16 by the 0.3. These are the values reported in Table 1.

Note that if we use our experimental S_e values (Table 1) to back-calculate D_{AB} for DEMP and DIMP, we obtain values of 0.029 and 0.023 cm^2/sec, respectively, which are probably at least as accurate and reliable as the those calculated using the approach described above. The lack of published D_{AB} values for organophosphonates such as these and of a reliable means of calculating them is an unfortunate situation that merits further study and resolution.

S9. Tests with vapor mixtures

Table S6 lists the concentrations, collected masses, exposure times, and observed Se and DE values for o-xylene and DEMP for the tests involving exposures to mixtures of these two compounds with and without other compounds present. In the case of the 8-compound mixture, data for all 8 compounds are provided in Table S7.

Table S6. Results of exposures to to o-xylene and DEMP individually and in various mixtures showing no effect on observed S_e values from the presence of other vapors.

Test	Compound	Conc. (mg/m^3)	Collected mass (ng)	Exposure time (min)	S_e (mL/min)	DE (%)
Single cmpd	o-xylene	42	440	15	0.69	99
	DEMP	49	190	15	0.26	91
2-cmpd mixture	o-xylene	370	7,500	30	0.68	99
	DEMP	87	660	30	0.25	87
5-cmpd mixture	o-xylene	110	2,200	30	0.68	99
	DEMP	14	110	30	0.26	88
8-cmpd mixture	o-xylene	6.2	130	30	0.71	99
	DEMP	9.0	68	30	0.25	80

Table S7. Results of exposures to eight compounds individually and as a mixture showing no effect on observed S_e values from the presence of other vapors.

Test	Compound	Conc. (mg/m^3)	Collected mass (ng)	Exposure time (min)	S_e (mL/min)	DE (%)
Individual cmpds	m-xylene	44	420	15	0.65	99

	cyclohexanol	42	390	15	0.62	98
	CEES	36	380	15	0.67	97
	cyclohexanone	23	240	15	0.64	96
	DMMP	24	160	15	0.44	98
	DIMP[a]	19	120	15	0.21	90
8-cmpd mixture	m-xylene	6.0	120	30	0.68	99
	cyclohexanol	1.9	37	30	0.62	98
	CEES	2.9	63	30	0.70	99
	cyclohexanone	12	250	30	0.65	99
	DMMP	6.0	76	30	0.42	84
	DIMP	6.6	45	30	0.22	82

[a] *These DIMP data were obtained from the 5-compound mixture test.*

References

S1. J. S. Mitchell, G. R. Lahiji and K. Najafi, *Proceedings of International Electronic Packaging Technical Conference and Exhibition (IPACK) '05*, July 17-22, 2005, San Francisco, CA, pp. 2041-2045

S2. J. Bryant-Genevier and E. T. Zellers, *J. Chromatogr. A*, 2015, **1422**, 299-309.

S3. G. O. Wood, *Carbon*, 1992, **30**, 593-599.

S4. F. Rouquerol, J. Rouquerol, K. S. W. Sing, P. Llewellyn and G. Maurin, *Adsorption by powders and porous solids: principles, methodology and applications*, Academic press, New York, 2013.

S5. Y.C. Chuang, P. C. Chiang and E. Chang, *Chemosphere*, 2003, **53**, 17-27.

S6. K.-J. Kim, C.-S. Kang, Y.-J. You, M.-C. Chung, M.-W. Woo, W.-J. Jeong, N.-C. Park and H.-G. Ahn, *Catalysis Today*, 2006, **111**, 223-228.

S7. F. D. Yu, L. A. Luo and G. Grevillot, *Journal of Chemical & Engineering Data*, 2002, **47**, 467-473.

S8. F.-Y. Yi, X.-D. Lin, S.-X. Chen and X.-Q. Wei, *Journal of Porous Materials*, 2009, **16**, 521-526.

S9. J. Wang, J. Ma and E. T. Zellers, *J. Chromatogr. A*. **1609**, 2020, 460486

S10. M. Tang, M. Shiraiwa, U. Pöschl, R. Cox and M. Kalberer, *Atmospheric Chemistry and Physics*, 2015, **15**, 5585-5598.

S11. G. Lugg, *Analytical Chemistry*, 1968, **40**, 1072-1077.

S12. J. T. Hunter and N. L. Abbott, *Sensors and Actuators B: Chemical*, 2013, **183**, 71-80.

S13. E. N. Fuller, P. D. Schettler and J. C. Giddings, *Industrial & Engineering Chemistry*, 1966, **58**, 18-27.

S14. E. N. Fuller, K. Ensley and J. C. Giddings, *The Journal of Physical Chemistry*, 1969, **73**, 3679-3685.

S15. D. A. Trubitsyn and A. V. Vorontsov, *The Journal of Physical Chemistry B*, 2005, **109**, 21884-21892.

S16. pubChem, https://pubchem.ncbi.nlm.nih.gov/ (accessed December 2019).

S17. VEGA ZZ, https://nova.disfarm.unimi.it/manual/pages/gl_index.htm (accessed December 2019).